Hamburger Beiträge
zur Angewandten Mathematik

Kernel-based Image Reconstruction from Scattered Radon Data

Stefano De Marchi, Armin Iske, Amos Sironi

Nr. 2016-11
May 2016

PADOVA UNIVERSITY PRESS

Dolomites Research Notes on Approximation

Volume 9 · 2016 · Pages 1–12

Kernel-based Image Reconstruction from Scattered Radon Data

Stefano De Marchi[a] · Armin Iske[b] · Amos Sironi[c]

Abstract

Computerized tomography requires suitable numerical methods for the approximation of a bivariate function f from a finite set of discrete Radon data, each of whose data samples represents one line integral of f. In standard reconstruction methods, specific assumptions concerning the geometry of the Radon lines are usually made. In relevant applications of image reconstruction, however, such assumptions are often too restrictive. In this case, one would rather prefer to work with reconstruction methods allowing for arbitrary distributions of scattered Radon lines.
This paper proposes a novel image reconstruction method for scattered Radon data, which combines kernel-based scattered data approximation with a well-adapted regularization of the Radon transform. This results in a very flexible numerical algorithm for image reconstruction, which works for arbitrary distributions of Radon lines. This is in contrast to the classical filtered back projection, which essentially relies on a regular distribution of the Radon lines, e.g. parallel beam geometry. The good performance of the kernel-based image reconstruction method is illustrated by numerical examples and comparisons.

1 Introduction

Computed Axial Tomography (CAT or CT) is a powerful technique to generate images from measurements of X-ray scans. One X-ray scan typically consists of several million of data samples, each of which corresponds to an X-ray beam passing through the computational domain, travelling from an emitter to a detector. The sensors of the operational CT scanner (positioned at the emitter and at the detector) then measures, for each X-ray beam, the loss of energy, resulting from the X-ray beam passing through the medium. The loss of energy reflects the ability of the medium to absorb energy, and so it depends on its specific structure and material properties. The amount of absorption can be described as a function of the computational domain Ω, termed *attenuation coefficient function*, $f : \Omega \to [0, \infty)$.

Medical imaging is one relevant application for CT, where the primary goal is to reconstruct the unknown attenuation coefficient function f from given X-ray scans in order to generate clinically useful medical images. This requires robust numerical algorithms to reconstruct characteristic features of medical images at sufficiently high accuracy, on the one hand, and at sufficiently small computational costs, on the other hand. For details concerning the acquisition of X-ray scans, their underlying mathematical models, and standard computational methods for medical image reconstruction, we refer to the textbook [5] of Feeman.

To describe the mathematical problem of medical image reconstruction from X-ray scans, let us first regard the *Radon transform* $\mathcal{R}f$ of f, given by

$$\mathcal{R}f(t,\theta) = \int_{\mathbb{R}} f(t\cos\theta - s\sin\theta, t\sin\theta + s\cos\theta)\, ds \tag{1}$$

for $t \in \mathbb{R}$ and $\theta \in [0,\pi)$, where we assume $f : \Omega \to \mathbb{R}$ to be a bivariate function on a compact domain $\Omega \subset \mathbb{R}^2$, or, in other words, we assume that f is compactly supported on $\mathbb{R}^2$, where we extend f to $\mathbb{R}^2$ by letting $f \equiv 0$ outside Ω. In many relevant application scenarios, we may assume that the image domain Ω is the unit square, i.e., $\Omega = [0,1]^2$, but this restriction is rather immaterial for our following discussion. We will merely assume $f \in L^1$, so that for any pair of $t \in \mathbb{R}$ and $\theta \in [0,\pi)$ the Radon integral in (1) is well-defined.

We remark that the Radon transform $\mathcal{R}f(t,\theta)$ gives, for any fixed pair $(t,\theta) \in \mathbb{R} \times [0,\pi)$, a line integral for f over a specific straight line $\ell \equiv \ell_{t,\theta}$. In order to see this, let $\ell_{t,\theta} \subset \mathbb{R}^2$ denote the unique straight line, which is perpendicular to unit vector $\mathbf{n}_\theta = (\cos\theta, \sin\theta)$ and which passes through point $p = (t\cos\theta, t\sin\theta) = t\mathbf{n}_\theta$. In this case, the line $\ell_{t,\theta}$ can be parameterized as

$$(x_1(s), x_2(s)) = (t\cos\theta - s\sin\theta, t\sin\theta + s\cos\theta). \tag{2}$$

By this specific choice for a parameterization of $\ell_{t,\theta}$ in (2), we immediately see that, for $t \in \mathbb{R}$ and $\theta \in [0,\pi)$,

$$\int_{\ell_{t,\theta}} f(\mathbf{x})\, d\mathbf{x} = \mathcal{R}f(t,\theta),$$

where we let $\mathbf{x} = (x_1, x_2)$, and so the line integral of f over $\ell_{t,\theta}$ coincides with the Radon transform (1) of f at (t,θ).

On the other hand, any straight line ℓ in the plane can be described by a unique pair (t,θ) of a radial parameter $t \in \mathbb{R}$ and an angular parameter $\theta \in [0,\pi)$ satisfying $\ell \equiv \ell_{t,\theta}$. In this way, the Radon transform $\mathcal{R}f$ of f can be viewed as a linear integral

[a] Department of Mathematics, University of Padua, Italy, demarchi@math.unipd.it
[b] Department of Mathematics, University of Hamburg, Germany, iske@math.uni-hamburg.de
[c] CVLab, EPFL, Lausanne, Switzerland, amos.sironi@epfl.ch

transformation, which maps any bivariate function $f \in L^1$ (in Cartesian coordinates) onto a bivariate function $\mathcal{R}f$ (in polar coordinates), where the image $\mathcal{R}f$ contains all line integrals of f over the set of straight lines in the plane.

Due the seminal work [12] of Johann Radon (in 1917), any (sufficiently regular) function f can be reconstructed from its Radon transform $\mathcal{R}f$. The inversion of the Radon transform is given by the *filtered back projection* (FBP) formula (see [5, Chapter 6]),

$$f(\mathbf{x}) = \frac{1}{2}\mathcal{B}\left\{\mathcal{F}^{-1}\left[|S|\mathcal{F}(\mathcal{R}f)(S,\theta)\right]\right\}(\mathbf{x}), \tag{3}$$

where $\mathcal{F}$ is, for any fixed angle θ, the *univariate* Fourier transform w.r.t. the radial variable t, and so is $\mathcal{F}^{-1}$ the univariate inverse Fourier transform w.r.t. the frequency variable S. Moreover, the *back projection* $\mathcal{B}$ is, for any function $h \equiv h(t,\theta)$ (in polar coordinates), given by the average

$$\mathcal{B}h(\mathbf{x}) = \frac{1}{\pi}\int_0^{\pi} h(x_1\cos\theta + x_2\sin\theta, \theta)\, d\theta$$

of $h(t,\theta)$ over the angular variable θ, where we let

$$t = x_1\cos\theta + x_2\sin\theta = \mathbf{x}\cdot\mathbf{n}_\theta \tag{4}$$

according to the one-to-one relation between the Cartesian coordinates $\mathbf{x} = (x_1, x_2)$ and the polar coordinates (t,θ), as described above along with the parameterization of the lines $\ell_{t,\theta}$ in (2). For basic details concerning the derivation of the filtered back projection formula, we refer to [5], and for a more comprehensive mathematical treatment of the Radon transform and its inversion, we refer to the textbooks [7, 10].

In practical application scenarios, however, only a *finite* set of Radon data,

$$\mathcal{R}_{\mathcal{L}}(f) = \{\mathcal{R}f(t_k,\theta_k)\}_{k=1}^m, \tag{5}$$

given as integrals of f over a finite set of m pairwise distinct lines,

$$\mathcal{L} = \{\ell_{t_k,\theta_k} : (t_k,\theta_k) \in \mathbb{R}\times[0,\infty) \text{ for } k = 1,\dots,m\},$$

is available. In this case, an approximate reconstruction of f from Radon data $\mathcal{R}_{\mathcal{L}}f$ is sought. In standard techniques of medical imaging, the reconstruction of f is accomplished by using a suitable discretization of the FBP in (3). For this class of Fourier-based reconstruction methods, the discrete lines in $\mathcal{L}$, over which the line integrals of f are known, are usually required to be regularly spaced in the plane, e.g. by assuming *parallel beam geometry* or *fan beam geometry* (see [5] for the geometric assumptions on $\mathcal{L}$).

In many clinical scenarios of data acquisition, however, we may face a limited range of angles or a limited dosage of X-ray expositions, so that the Radon data are partly corrupt or incomplete. In such relevant cases, the Radon data in (5) are *scattered*, i.e., the distribution of lines in $\mathcal{L}$ is essentially *not* regular but scattered, in which case standard Fourier methods, such as the Fourier-based FBP discretization in (3), do no longer apply. This requires more flexible approximation methods which work for arbitrary geometries of (scattered) Radon lines $\mathcal{L}$.

To approximate f from *scattered* Radon data $\mathcal{R}_{\mathcal{L}}f$, *algebraic reconstruction techniques* (ART) [6] can be applied. The concept of ART is essentially different from that of Fourier-based reconstructions: in the setting of ART one fixes a set $\mathcal{G} = \{g_j\}_{j=1}^n$ of basis functions beforehand to solve the reconstruction problem

$$\mathcal{R}_{\mathcal{L}}(g) = \mathcal{R}_{\mathcal{L}}(f) \tag{6}$$

by using a linear combination

$$g = \sum_{j=1}^n c_j g_j$$

of the basis functions in $\mathcal{G}$. This ansatz amounts to solving the linear system

$$Ac = b \tag{7}$$

for the unknown coefficients $c = (c_1,\dots,c_n)^T \in \mathbb{R}^n$ of g, where the $m\times n$ matrix A has the form

$$A = \big(\mathcal{R}g_j(t_k,\theta_k)\big)_{k=1,\dots,m;\, j=1,\dots,n} \in \mathbb{R}^{m\times n}$$

and the right hand side b is given by the m Radon observations $b_k = \mathcal{R}f(t_k,\theta_k)$, for $k = 1,\dots,m$.

Unless the number m of Radon samples coincides with the number n of coefficients, the linear system in (7) is either overdetermined, for $m > n$, or underdetermined, for $n > m$. In case of an overdetermined system, the classical method of *linear least squares approximation* [2] is applied to minimize the residual (Euclidean) norm $\|Ac - b\|$, whereas for an underdetermined system the iterative method of Kaczmarz [5, Section 9.3] is a standard tool to compute an approximate solution c satisfying $Ac \approx b$. We remark that in either case the linear system in (7) is not guaranteed to have a unique solution, not even in the rare case, where $m = n$. In fact, the latter is due to the *Mairhuber theorem* [4, Chapter 1] from multivariate approximation theory.

In this paper, we propose a kernel-based algebraic reconstruction method, whose solution is always unique. Our proposed reconstruction scheme relies on the concept of kernel-based multivariate approximation from generalized Hermite-Birkhoff data [8], which we adapt to the special case of reconstruction from scattered Radon data. For the well-posedness of the reconstruction scheme we apply weighted Radon transforms for the purpose of regularization, as explained later in this paper. This way we obtain a very flexible reconstruction scheme, which works for arbitrary scattered Radon data.

The outline of this paper is as follows. In the following Section 2, we briefly review generalized Hermite-Birkhoff interpolation, where we show how to adapt this particular reconstruction method to scattered Radon data. This is followed by a discussion on the regularization of the Radon transform in Section 5, where we work with weighted Radon transforms. In Section 6, numerical results are finally provided for illustration. Our numerical experiments of Section 6 include comparisons between Fourier-based reconstructions relying on the FBP formula (3) and the kernel-based ART proposed in this paper, where we apply the two reconstructions methods to three popular phantoms.

2 Generalized Hermite-Birkhoff Interpolation

To solve the reconstruction problem (6), we consider applying Hermite-Birkhoff interpolation [8]. To explain the general framework of this particular interpolation method, let $\Lambda = \{\lambda_1, \dots, \lambda_n\}$ denote a set of linearly independent linear functionals. Moreover, suppose we are given a vector $f_\Lambda = (\lambda_1(f), \dots, \lambda_n(f))^T \in \mathbb{R}^n$ of samples taken from an unknown function f. Now the solution of the general Hermite-Birkhoff reconstruction problem requires finding a function g satisfying the interpolation conditions $g_\Lambda = f_\Lambda$, i.e.,

$$\lambda_k(g) = \lambda_k(f) \qquad \text{for all } k = 1, \dots, n. \tag{8}$$

This general framework covers our reconstruction problem (6), when the linear functionals λ_k are defined as

$$\lambda_k(f) := \mathcal{R}f(t_k, \theta_k) \qquad \text{for } k = 1, \dots, n. \tag{9}$$

By the interpolation conditions in (8), we obtain n linear equations of the form

$$\sum_{j=1}^{n} c_j \lambda_k(g_j) = \lambda_k(f) \qquad \text{for } k = 1, \dots, n,$$

corresponding to the linear system in (7), and by the choice of our particular ansatz, the number of data matches the number of basis functions, i.e., $n = m$. To obtain a well-posed reconstruction scheme, we assume that the basis functions g_j are of the form

$$g_j(\mathbf{x}) = \lambda_j^{\mathbf{y}} K(\mathbf{x}, \mathbf{y}) \qquad \text{for } j = 1, \dots, n, \tag{10}$$

where $\lambda_j^{\mathbf{y}} K(\mathbf{x}, \mathbf{y})$ denotes action of the functional λ_j to K w.r.t. variable $\mathbf{y} \in \mathbb{R}^2$. Moreover, the kernel function $K \equiv K(\mathbf{x}, \mathbf{y})$ is required to be *symmetric*, i.e.,

$$K(\mathbf{x}, \mathbf{y}) = K(\mathbf{y}, \mathbf{x}) \quad \text{for all } \mathbf{x}, \mathbf{y} \in \mathbb{R}^2,$$

and *positive definite*.

Rather than dwelling much on explaining positive definite functions, we remark that for the purposes of this paper it is sufficient to say that a symmetric function $K \equiv K(\mathbf{x}, \mathbf{y})$ is *positive definite*, iff the matrix

$$A_{\Lambda,K} = \left(\lambda_j^{\mathbf{x}} \lambda_k^{\mathbf{y}} K(\mathbf{x}, \mathbf{y}) \right)_{1 \le j,k \le n} \in \mathbb{R}^{n \times n} \tag{11}$$

is symmetric positive definite for any set $\Lambda = \{\lambda_j\}_{j=1}^n$ of linearly independent functionals λ_j. For a comprehensive account to the construction and characterization of positive definite kernels, we refer the reader to [9, 13].

To make relevant examples for positive definite kernels, we resort to radially symmetric kernels, in which case K is assumed to have the form

$$K(\mathbf{x}, \mathbf{y}) = \phi(\|\mathbf{x} - \mathbf{y}\|) \qquad \text{for } \mathbf{x}, \mathbf{y} \in \mathbb{R}^2,$$

where $\phi(\|\cdot\|)$ is radial w.r.t. the Euclidean norm $\|\cdot\|$. Classical choices for radial kernels are the *Gaussians*

$$\phi_\varepsilon(\|\mathbf{x}\|) = e^{-(\varepsilon\|\mathbf{x}\|)^2} \quad \text{for } \mathbf{x} \in \mathbb{R}^2 \text{ and } \varepsilon > 0,$$

which are for any $\varepsilon > 0$ positive definite, i.e.,

$$K(\mathbf{x}, \mathbf{y}) = \exp(-(\varepsilon\|\mathbf{x} - \mathbf{y}\|)^2) \tag{12}$$

is positive definite. Other popular examples for radial positive definite kernels are the *inverse multiquadrics*

$$\phi_\varepsilon(\|\mathbf{x}\|) = \left(1 + (\varepsilon\|\mathbf{x}\|)^2\right)^{-1/2} \quad \text{for } \mathbf{x} \in \mathbb{R}^2 \text{ and } \varepsilon > 0,$$

and Askey's compactly supported *radial characteristic functions* [1],

$$\phi_\varepsilon(\|\mathbf{x}\|) = (1 - \varepsilon\|\mathbf{x}\|)_+^\beta = \begin{cases} (1 - \varepsilon\|\mathbf{x}\|)^\beta & \text{for } \|\mathbf{x}\| < 1/\varepsilon \\ 0 & \text{for } \|\mathbf{x}\| \ge 1/\varepsilon \end{cases}$$

which are positive definite for any $\beta > 3/2$.

In the following discussion, we show that Gaussian kernels are suitable choices for ϕ_ε, especially for reconstructions from *Radon data*, where we need to assembly the reconstruction matrix $A \equiv A_{\Lambda,K}$ in (11) by applying the Radon transform $\mathcal{R}$ on the chosen kernel K.

Our preference for the Gaussian kernel is also supported by our extensive numerical experiments in [14], where we have observed that the approximation quality of Gaussian reconstruction is superior to that of other commonly used positive definite kernels. This complies with available error estimates for (plain) Lagrange interpolation by Gaussian kernels [15, Section 11.3], which are shown to provide spectral convergence orders.

3 Construction of the Basis Functions

We remark that the basis functions g_j in (10) are rather straightforward to compute. In the case of the inverse multiquadrics, however, the basis functions g_j are not well-defined. In fact, note that the Radon transform

$$\mathcal{R}^y K(x,y)(t,\theta) = \int_{\mathbb{R}} K(x,(t\cos(\theta)-s\sin(\theta),t\sin(\theta)+s\cos(\theta)))\,ds \tag{13}$$

of the basis functions g_j in (10) may be undefined for specific choices of $(t,\theta)\in\mathbb{R}\times[0,\pi)$ and $x\in\mathbb{R}^2$. Indeed, in this case, we have

$$K(x,(t\cos(\theta)-s\sin(\theta),t\sin(\theta)+s\cos(\theta))) = \mathcal{O}(s^{-1})$$

for $s\to\pm\infty$, so that the integral in (14) is singular for any $(t,\theta)\in\mathbb{R}\times[0,\pi)$ and $x\in\mathbb{R}^2$.

To solve this problem, we apply a *Gabor transform*, with window function

$$G_\sigma(r) = \frac{1}{\sqrt{2\pi}\sigma}\exp\left(-\frac{r^2}{2\sigma^2}\right) \qquad \text{for } \sigma>0,$$

to the kernel $K(x,y)=\phi_\varepsilon(\|x-y\|)$, i.e., we replace the inverse multiquadrics ϕ_ε by the *windowed* inverse multiquadrics kernel

$$\phi_{\varepsilon,\sigma}(r) := \phi_\varepsilon(r)G_\sigma(r),$$

where the width $2\sigma>0$ of the Gabor window G_σ is chosen to match the diameter of the computational domain, i.e., we let $\sigma := \operatorname{diam}(\Omega)/2$. Note that $\phi_{\varepsilon,\sigma}$ is positive definite, since each factor, ϕ_ε and G_σ, is positive definite, i.e., $\phi_{\varepsilon,\sigma}$ is for any $\varepsilon,\sigma>0$ a positive definite radial kernel function. In this way, we obtain a well-defined integral (14), since the integrand

$$K(x,y)=\phi_{\varepsilon,\sigma}(\|x-y\|) = \frac{1}{\sqrt{2\pi}\sigma}\,\frac{\exp\left(-\frac{\|x-y\|^2}{2\sigma^2}\right)}{\sqrt{1+(\varepsilon\|x-y\|)^2}}$$

is for any $x\in\mathbb{R}^2$ in $L^1(\mathbb{R}^2)$ w.r.t. variable

$$y\equiv y(s) = (t\cos(\theta)-s\sin(\theta),t\sin(\theta)+s\cos(\theta)).$$

Note that for the other two examples of kernel functions, i.e., for the Gaussians and for the compactly supported radial kernels, this problem does not occur. Indeed, in either of these two cases, we have $\phi_\varepsilon(r)\in L^1([0,\infty))$, so that the function $K(x,\cdot)=\phi_\varepsilon(\|x-\cdot\|)$ is, for any $\varepsilon>0$ and $x\in\mathbb{R}^2$, integrable over $\mathbb{R}^2$. In particular, the integral in (14) is in this case well-defined for any combination of $(t,\theta)\in\mathbb{R}\times[0,\pi)$ and $x\in\mathbb{R}^2$, and so the basis functions g_j in (10) are well-defined.

For all of the three abovementioned examples – Gaussians, inverse multiquadrics (with using Gabor transform) and compactly supported radial kernels – we have computed the basis functions g_j in (10). This is done in all details in [14]. For the compactly supported radial kernels, the basis functions are found in of [14, § 5.4.1], and for the inverse multiquadrics they are computed in [14, § 5.2]. For instance, the basis functions for the compactly supported kernel $\phi_\varepsilon(r)=(1-\varepsilon r)_+^2$ are given as

$$g_j(x) = (\mathcal{R}^y K(x,y))(t_j,\theta_j) = \begin{cases} h(t_j-x\cdot\mathbf{n}_j) & \text{for } |t_j-x\cdot\mathbf{n}_j|\le 1/\varepsilon,\\ 0 & \text{for } |t_j-x\cdot\mathbf{n}_j|>1/\varepsilon,\end{cases}$$

where $\mathbf{n}_j=(\cos(\theta_j),\sin(\theta_j))$, and where

$$h(t) = \begin{cases} \frac{2}{\varepsilon}\left[\frac{\sqrt{1-(\varepsilon t)^2}}{3}(2(\varepsilon t)^2+1)-(\varepsilon t)^2\operatorname{acosh}(\varepsilon^{-1}|t|^{-1})\right] & \text{for } t\neq 0,\\ \frac{2}{3\varepsilon} & \text{for } t=0.\end{cases}$$

We decided to omit the tedious details of the required computations for the two cases of the inverse multiquadrics and compactly supported radial kernel, but rather refer to [14]. For the purposes of this paper, it is sufficient and quite instructive to show how the computations for the Gaussian kernels are done. This is discussed in the next section.

4 Construction of the Gaussian Basis Functions

Let $K(\mathbf{x},\mathbf{y})=\phi_\varepsilon(\|\mathbf{x}-\mathbf{y}\|)$ denote the Gaussian kernel in (12). To discuss the assembly of the reconstruction matrix A in (11), let us first compute the Gaussian basis functions $g_j(\mathbf{x})=\mathcal{R}^y K(\mathbf{x},\mathbf{y})(t_j,\theta_j)$ in (10).

To this end, note that $\phi_\varepsilon(r)\in L^1([0,\infty))$, and so the Radon transform

$$\mathcal{R}^y K(\mathbf{x},\mathbf{y})(t,\theta) = \int_{\mathbb{R}} K(\mathbf{x},\mathbf{y}(s,t,\theta))\,ds \tag{14}$$

where $\mathbf{y}(s,t,\theta)=(t\cos(\theta)-s\sin(\theta),t\sin(\theta)+s\cos(\theta))$, is for any combination of $(t,\theta)\in\mathbb{R}\times[0,\pi)$ and $\mathbf{x}\in\mathbb{R}^2$ well-defined, i.e., the Gaussian basis functions g_j are well-defined. Note that this is in contrast to reconstruction by inverse multiquadrics, where the integral in (14) is singular for any $(t,\theta)\in\mathbb{R}\times[0,\pi)$ and $\mathbf{x}\in\mathbb{R}^2$.

For the following of our analysis it will be convenient to use the *shift property* of the Radon transform.

Lemma 4.1. *Let $K(\mathbf{x},\mathbf{y}) = \phi(\|\mathbf{x}-\mathbf{y}\|)$ with $\phi \in L^1(\mathbb{R})$. Then, for any $\mathbf{x} \in \mathbb{R}^2$ the Radon transform $\mathcal{R}^{\mathbf{y}}K(\mathbf{x},\mathbf{y})$ at $(t,\theta) \in \mathbb{R}\times[0,\pi)$ can be expressed as*

$$(\mathcal{R}^{\mathbf{y}}K(\mathbf{x},\mathbf{y}))(t,\theta) = (\mathcal{R}^{\mathbf{y}}K(\mathbf{0},\mathbf{y}))(t-\mathbf{x}\cdot\mathbf{n}_\theta,\theta), \tag{15}$$

where $\mathbf{n}_\theta = (\cos\theta,\sin\theta)$.

Although this is a rather standard fact about Radon transforms [7], we provide a short proof of this property.

Proof. First note that identity (15) can be rewritten as

$$\int_{\ell_{t,\theta}} \phi(\|\mathbf{y}-\mathbf{x}\|)\,d\mathbf{y} = \int_{\ell_{t-\mathbf{x}\cdot\mathbf{n}_\theta,\theta}} \phi(\|\mathbf{z}\|)\,d\mathbf{z}.$$

To see this is true, further note that $\mathbf{y} = (y_1,y_2) \in \ell_{t,\theta}$ implies

$$t = \mathbf{y}\cdot\mathbf{n}_\theta = y_1\cos\theta + y_2\sin\theta$$

from (4). But this in turn yields $\mathbf{y}-\mathbf{x} \in \ell_{t-\mathbf{x}\cdot\mathbf{n}_\theta,\theta}$, since

$$t-\mathbf{x}\cdot\mathbf{n}_\theta = \mathbf{y}\cdot\mathbf{n}_\theta - \mathbf{x}\cdot\mathbf{n}_\theta = (\mathbf{y}-\mathbf{x})\cdot\mathbf{n}_\theta.$$

In other words, for $\mathbf{y} \in \ell_{t,\theta}$, we see that $\ell_{t-\mathbf{x}\cdot\mathbf{n}_\theta,\theta}$ is, for fixed θ, the unique straight line passing through $\mathbf{y}-\mathbf{x}$. □

Now we are in a position to compute the *Gaussian basis functions* $g_j = (\mathcal{R}^{\mathbf{y}}K(\cdot,\mathbf{y}))(t_j,\theta_j)$ in (10).

Theorem 4.2. *For any $(t,\theta) \in \mathbb{R}\times[0,\pi)$, the Gaussian basis function $g \equiv g(t,\theta)$ is given as*

$$g(\mathbf{x}) = (\mathcal{R}^{\mathbf{y}}K(\mathbf{x},\mathbf{y}))(t,\theta) = \frac{\sqrt{\pi}}{\varepsilon}e^{-\varepsilon^2(t-\mathbf{x}\cdot\mathbf{n}_\theta)^2}, \tag{16}$$

where $\mathbf{n}_\theta = (\cos\theta,\sin\theta)$.

Proof. For the Radon transform $\mathcal{R}K_{\mathbf{0}}$ of $K_{\mathbf{0}}(\mathbf{y}) = K(\mathbf{0},\mathbf{y})$ at $(t,\theta) \in \mathbb{R}\times[0,\pi)$ we get

$$\begin{aligned}
\mathcal{R}K_{\mathbf{0}}(t,\theta) &= \int_{\ell_{t,\theta}} K_{\mathbf{0}}(\mathbf{y})\,d\mathbf{y} = \int_{\mathbb{R}} K_{\mathbf{0}}(t\cos\theta - s\sin\theta,\, t\sin\theta + s\cos\theta)\,ds \\
&= \int_{\mathbb{R}} e^{-\varepsilon^2(t\cos\theta-s\sin\theta)^2-\varepsilon^2(t\sin\theta+s\cos\theta)^2}\,ds = \int_{\mathbb{R}} e^{-\varepsilon^2(t^2+s^2)}\,ds = e^{-(\varepsilon t)^2}\int_{\mathbb{R}} e^{-(\varepsilon s)^2}\,ds \\
&= \frac{\sqrt{\pi}}{\varepsilon}e^{-\varepsilon^2 t^2},
\end{aligned}$$

which in turn yields the Gaussian basis function

$$(\mathcal{R}^{\mathbf{y}}K(\mathbf{x},\mathbf{y}))(t,\theta) = (\mathcal{R}^{\mathbf{y}}K_{\mathbf{0}})(t-\mathbf{x}\cdot\mathbf{n}_\theta,\theta) = \frac{\sqrt{\pi}}{\varepsilon}e^{-\varepsilon^2(t-\mathbf{x}\cdot\mathbf{n}_\theta)^2}$$

from the Radon transform's shift property, Lemma 4.1. □

Now let us turn to the entries of the reconstruction matrix $A = (a_{kj})_{1\le j,k\le n}$ in (11). Note that the matrix entry a_{kj} is given by the application of the Radon transform $\mathcal{R} \equiv \mathcal{R}(t_k,\theta_k)$ to the basis function $g_j = \mathcal{R}^{\mathbf{y}}K(\cdot,\mathbf{y})(t_j,\theta_j)$, so that

$$a_{kj} = \mathcal{R}^{\mathbf{x}}[(\mathcal{R}^{\mathbf{y}}K(\mathbf{x},\mathbf{y}))(t_j,\theta_j)](t_k,\theta_k). \tag{17}$$

We can compute the entries of matrix A as follows.

Theorem 4.3. *For the Gaussian kernel ϕ_ε, the entries (17) of the reconstruction matrix A are given as*

$$a_{kj} = \frac{\pi}{\varepsilon^2\sin(\theta_k-\theta_j)}. \tag{18}$$

Proof. We let $(t,\theta) := (t_j,\theta_j)$ and $(r,\varphi) := (t_k,\theta_k)$ for the sake of notational simplicity. Recalling the form of the Gaussian basis function in (16), we can compute the entry a_{kj} by

$$\begin{aligned}
\mathcal{R}^{\mathbf{x}}\left[e^{-(t-\mathbf{x}\cdot\mathbf{n}_\theta)^2}\right](r,\varphi) &= \int_{\mathbb{R}} e^{-[t-(r\cos\varphi-s\sin\varphi)\cos\theta-(r\sin\varphi+s\cos\varphi)\sin\theta]^2}\,ds \\
&= \int_{\mathbb{R}} e^{-[t-r(\cos\varphi\cos\theta+\sin\varphi\sin\theta)+s(\sin\varphi\cos\theta-\cos\varphi\sin\theta)]^2}\,ds \\
&= \int_{\mathbb{R}} e^{-[t-r\cos(\varphi-\theta)+s\sin(\varphi-\theta)]^2}\,ds \\
&= \int_{\mathbb{R}} e^{-[as+b]^2}\,ds,
\end{aligned}$$

where we let $a := \sin(\varphi-\theta)$ and $b := t - r\cos(\varphi-\theta)$. Hence, for $a \neq 0$, we get

$$a_{kj} = \mathcal{R}^{\mathbf{x}}\left[\frac{\sqrt{\pi}}{\varepsilon}e^{-\varepsilon^2(t-\mathbf{x}\cdot\mathbf{n}n_\theta)^2}\right](r,\varphi) = \frac{\sqrt{\pi}}{\varepsilon}\int_{\mathbb{R}} e^{-\varepsilon^2[as+b]^2}\,ds = \frac{\pi}{\varepsilon^2 a} = \frac{\pi}{\varepsilon^2\sin(\varphi-\theta)}$$

as stated. □

Note that the above entries a_{kj} do not depend on the radial parameters, t_j and t_k, but only on the angular parameters, θ_j and θ_k. This is due to the radial symmetry of the Gaussian kernel K.

For different angles $\theta_j, \theta_k \in [0,\pi)$, $\theta_j \neq \theta_k$, the entry a_{kj} of A in (18) is well-defined. For coincident angles $\theta_j = \theta_k$, however, the entry a_{kj} is singular, i.e., the Radon transform $a_{kj} = (\mathcal{R}(g_j))(t_k,\theta_k)$ is singular, iff the angular parameters of the Radon lines ℓ_{t_j,θ_j} and ℓ_{t_k,θ_k} coincide, i.e., iff $\theta_j = \theta_k$. So, in particular, are the diagonal entries of A in (11) singular.

5 Regularization by Gaussian Weights

To obtain non-singular entries in the reconstruction matrix A in (11), we require suitable regularizations for the Radon transform $\mathcal{R}$. To this end, we work with *weighted Radon transforms* of the form

$$\mathcal{R}_w f(t,\theta) := \mathcal{R}(fw)(t,\theta) = \int_{\ell_{t,\theta}} f(\mathbf{x})w(\mathbf{x})\,d\mathbf{x} \tag{19}$$

where $w \equiv w(\mathbf{x})$ is a fixed weight function. This yields a standard regularization for the Radon transform $\mathcal{R}$, which also arises in relevant applications of *single photon emission computed tomography* (SPECT), where $\mathcal{R}_w$ is called *attenuated Radon transform* [11].

As for the choice of the weight w, we prefer to use the radially symmetric Gaussian function

$$w_\nu(\mathbf{x}) = \exp(-(\nu\|\mathbf{x}\|)^2) \quad \text{for } \nu > 0. \tag{20}$$

This particular choice is well-motivated, since the product $\phi_\varepsilon \cdot w_\nu$ of the two positive definite Gaussians, ϕ_ε and w_ν, is positive definite, due to the classical Bochner theorem [3]. Indeed, according to Bochner's theorem, any function $f \in L^1$ with positive Fourier transform $\hat{f}$ is positive definite. Hence, for any pair of functions $f, g \in L^1$ with positive Fourier transforms $\hat{f}, \hat{g}$, their product $f \cdot g$ is positive definite, since their convolution $\hat{f} * \hat{g}$ (giving their Fourier transform) is positive.

In this way, the resulting reconstruction problem

$$\mathcal{R}_w g(t_k,\theta_k) = \mathcal{R}f(t_k,\theta_k) \quad \text{for all } k = 1,\dots,n,$$

assuming (10) for the form of the Gaussian basis functions, leads to a well-posed reconstruction scheme with reconstruction matrix

$$A \equiv A_w = \big(\mathcal{R}_w g_j(t_k,\theta_k)\big)_{1\le j,k\le n} \in \mathbb{R}^{n\times n}. \tag{21}$$

We compute the entries of A analytically as follows.

Theorem 5.1. *For the Gaussian kernel ϕ_ε, $\varepsilon > 0$, and the Gaussian weight w_ν, $\nu > 0$, the entries (21) of the reconstruction matrix $A_w = (a_{kj})_{1\le j,k\le n}$ are given as*

$$a_{kj} = \frac{\pi}{\varepsilon\sqrt{\varepsilon^2\alpha_{kj}^2+\nu^2}}\exp\left[-\nu^2\left(t_k^2 + \frac{\varepsilon^2\beta_{kj}^2}{\varepsilon^2\alpha_{kj}^2+\nu^2}\right)\right],$$

where $\beta_{kj} = t_j - t_k\cos(\theta_k-\theta_j)$ and $\alpha_{kj} = \sin(\theta_k-\theta_j)$.

Proof. For notational convenience, we let $(t,\theta) = (t_j,\theta_j)$ and $(r,\varphi) = (t_k,\theta_k)$. Recalling the representation of the Gaussian basis function $g \equiv g(t,\theta)$ in Theorem 4.2, we can compute the weighted Radon transform $\mathcal{R}_w g$ by following along the lines of our proof in Theorem 4.3, which yields

$$(\mathcal{R}_w g)(r,\varphi) = \int_{\mathbb{R}} g(\mathbf{x}(s))e^{-\nu^2\|\mathbf{x}(s)\|^2}\,ds = \frac{\sqrt{\pi}}{\varepsilon}\int_{\mathbb{R}} e^{-\varepsilon^2(as+b)^2}e^{-\nu^2(r^2+s^2)}\,ds,$$

where we let $a = \sin(\varphi-\theta)$ and $b = t - r\cos(\varphi-\theta)$, and where we have used the identity

$$\|\mathbf{x}(s)\|^2 = r^2+s^2 \qquad \text{for } \mathbf{x}(s) = (r\cos\varphi - s\sin\varphi,\, r\sin\varphi + s\cos\varphi).$$

This immediately yields the entries of A_w by

$$\begin{aligned}
(\mathcal{R}_w g)(r,\varphi) &= \frac{\sqrt{\pi}}{\varepsilon}e^{-\varepsilon^2b^2-\nu^2r^2}\int_{\mathbb{R}} e^{-[(\varepsilon^2a^2+\nu^2)s^2+2ab\varepsilon^2]}\,ds \\
&= \frac{\sqrt{\pi}}{\varepsilon}e^{-\varepsilon^2b^2-\nu^2r^2+\frac{a^2b^2\varepsilon^4}{\varepsilon^2a^2+\nu^2}}\int_{\mathbb{R}} e^{-\left[\sqrt{\varepsilon^2a^2+\nu^2}s+\frac{ab\varepsilon^2}{\sqrt{\varepsilon^2a^2+\nu^2}}\right]^2}\,ds \\
&= \frac{\pi}{\varepsilon\sqrt{\varepsilon^2a^2+\nu^2}}e^{-\nu^2\left(r^2+\frac{\varepsilon^2b^2}{\varepsilon^2a^2+\nu^2}\right)}.
\end{aligned}$$

□

Note that for any $\nu > 0$, the entries a_{kj} of A_w are well-defined, even for coincident angles θ_j and θ_k. Indeed, for $\theta_j = \theta_k$, we have $\alpha_{kj} = 0$, $\beta_{kj} = t_k - t_j$, and so in this case

$$a_{kj} = \frac{\pi}{\varepsilon\,\nu} \exp\left[-\nu^2\left(t_k^2 + \frac{\varepsilon^2(t_k - t_j)^2}{\nu^2}\right)\right].$$

6 Numerical Results

We have implemented the proposed kernel-based reconstruction scheme for the three kernels ϕ_ε — Gaussians, inverse multiquadrics, and compactly supported radial kernels — in combination with the Radon transform's regularization and by using the Gaussian weight function w_ν. We have performed quite comprehensive numerical experiments for various possible combinations of kernels ϕ_ε and weights w_ν, a selection of which we present here for the purpose of illustration.

In our series of numerical experiments concerning the popular phantoms *bull's eye*, the *crescent-shaped phantom*, and the *Shepp-Logan phantom*, we found that the Gaussian kernel performs much better than the inverse multiquadrics and the compactly supported kernel $\phi_\varepsilon(r) = (1-\varepsilon r)_+^2$, where the performance of the latter two kernels is comparable. This is supported by our numerical example in Figure 3. Indeed, we obtained the best numerical results – in terms of the reconstructions' visual quality and the root mean square error (RMSE) in (22) – for the Gaussian kernel $\phi_\varepsilon(r) = \exp(-(\varepsilon r)^2)$ in combination with the Gaussian weight function $w_\nu(x) = \exp(-(\nu\|x\|)^2)$, provided that the shape parameters ε and ν were properly chosen.

In fact, we found that the performance of the Gaussian reconstruction method is quite sensitive to the choice of the method parameters ε and ν. Therefore, we decided to perform a "fine-tuning" of the Gaussian parameters ε and ν, whose numerical results are presented in Subsection 6.2. Moreover, in Subsection 6.4 we provide numerical comparisons with Fourier-based reconstructions, relying on the filtered back projection formula, for Radon data on parallel beam geometry. In Subsection 6.5, we present numerical results concerning Gaussian reconstruction from *scattered* Radon data, and in Subsection 6.3 from *regular* Radon data (on parallel beam geometry), where we also provide a comparison between different kernels. Comparisons concerning Gaussian reconstruction on regular Radon data vs scattered Radon data are provided in the following Subsection 6.1. For a more comprehensive documentation on our numerical experiments, we refer to [14].

6.1 Reconstruction of the Crescent-Shaped Phantom

Let us first regard the popular test case *crescent-shaped phantom*, given by the function

$$f(x,y) = \begin{cases} 1.0 & \text{for } (x,y) \in \Omega, \\ 0.5 & \text{for } (x,y) \in D_i, \\ 0.0 & \text{for } (x,y) \in \mathbb{R}^2 \setminus D_o, \end{cases}$$

on the unit square $\Omega = [0,1]^2$, where

$$\begin{aligned} D_i &= \{(x,y) \in \mathbb{R}^2 : (x-1/8)^2 + y^2 \le 9/64\} \\ D_o &= \{(x,y) \in \mathbb{R}^2 : x^2 + y^2 \le 1/4\}, \end{aligned}$$

as shown in Figure 1 (a). Figures 1 (b),(c) show the reconstruction of the crescent-shaped phantom obtained with the Gaussian kernel ϕ_ε and the Gaussian weight function w_ν for parameters $\varepsilon = 40$ and $\nu = 0.7$, and for $n = 3888$ different Radon lines. The Radon samples were taken on a set of n regularly distributed lines generated by *parallel beam geometry*, and on a set of n *scattered* Radon lines. In either case, the crescent-shaped phantom f is localized and reconstructed fairly well by the proposed kernel-based reconstruction scheme. But the quality of the reconstruction on parallel beams, Figure 1 (b), is superior to that on scattered lines, Figure 1 (c). This is due to the uniform coverage of the Radon lines over the computational domain Ω. The geometry of the Radon lines are visible in the display of the reconstructions in Figures 1 (b),(c), especially between the boundary of the domain Ω and the phantom's boundary.

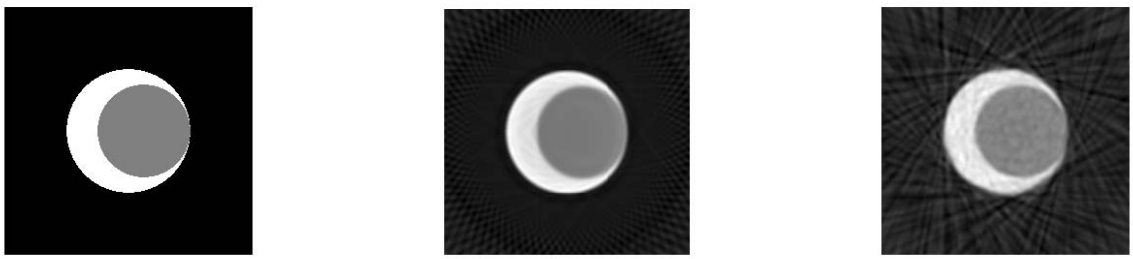

(a) crescent-shaped phantom (b) parallel beam geometry (c) scattered Radon data

Figure 1: Crescent-shaped phantom. (a) Original phantom; (b)-(c) reconstruction of crescent-shaped phantom using the Gaussian kernel ϕ_ε with $\varepsilon = 40$ and the Gaussian weight function w_ν with $\nu = 0.7$ from $n = 3888$ Radon samples taken on (b) regularly spaced Radon lines (parallel beam geometry), (c) scattered Radon lines.

6.2 Selection of the Gaussian Shape Parameters

In this subsection, we discuss the selection of the method parameters ε (for the Gaussian kernel ϕ_ε) and ν (for the Gaussian weight function w_ν), here applied to the phantom *bull's eye*, defined as

$$f(x,y) = \begin{cases} 1/2 & \text{iff } x^2+y^2 \le 1/16; \\ 1/4 & \text{iff } 1/16 < x^2+y^2 \le 1/4; \\ 1 & \text{iff } 1/4 < x^2+y^2 \le 9/16; \\ 0 & \text{iff } 9/16 < x^2+y^2. \end{cases}$$

The phantom bull's eye is displayed in Figure 3, second row, first column. In our numerical experiments, we have analyzed the behaviour of the Gaussian reconstruction error as a bivariate function of the parameters ε and ν. For the error measure, we consider using the standard *root mean square error*

$$\text{RMSE} = \sqrt{\frac{1}{J}\sum_{j=1}^{J}(f_j - \hat{f}_j)^2}, \tag{22}$$

where J is the size of the image (i.e., the number of pixels) and $\{f_j\}_{j=1}^J$, $\{\hat{f}_j\}_{j=1}^J$ are the greyscale values at the pixels of the original image bull's eye and of the reconstructed image, respectively.

Let us first consider the variation of the shape parameter ε of the Gaussian kernel ϕ_ε. In our numerical experiments, we have fixed the weight parameter at $\nu = 0.7$. For different choices of N and M, we have used parallel beam geometry with N angles and $2M+1$ parallel lines per angle, resulting in a number of $n = N \times (2M+1)$ Radon samples for each numerical experiment. With the variation of the shape parameter ε, we have recorded an "optimal" value ε^*, where, according to our numerical observations, the RMSE is minimal. The following Table 1 reflects our results. Note that the "optimal" value ε^* increases with the number n of Radon data taken. This is not too surprising insofar as in plain kernel-based interpolation, the shape parameter of the Gaussian kernel is recommended to be proportional to the density of the sample points: the higher the density of points, the larger ε should be chosen. In our numerical experiments, the sample density increases with the number n of lines, which explains the monotonicity of ε^* in Table 1.

N	36	54	72	90	108	126	144	162	180
M	20	30	40	50	60	70	80	90	100
n	1,476	3,294	5,832	9,090	13,068	17,766	23,184	29,322	36,180
ε^*	21.05	28.42	37.36	48.42	59.47	72.10	84.21	90.52	97.37

Table 1: Parameter-tuning for Gaussian kernel ϕ_ε. Reconstruction of phantom bull's eye by Gaussian kernel ϕ_ε, with variation of the kernel parameter ε. For fixed weight parameter $\nu = 0.7$, and for different choices of N angles θ and $2M+1$ lines per angle in a parallel beam geometry. For each experiment, the "optimal" shape parameter ε^*, whose resulting RMSE is minimal, is shown.

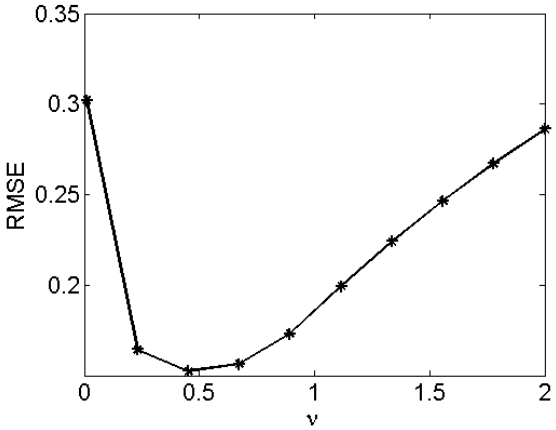

Figure 2: Parameter-tuning for Gaussian weight function w_ν. Reconstruction of phantom bull's eye by the Gaussian kernel $\phi_\varepsilon(r) = \exp(-(\varepsilon r)^2)$ for $\varepsilon = 30$. The graph of the RMSE as a function of the weight parameter ν is shown.

Next we consider the variation of the shape parameter ν for the Gaussian weight function w_ν in (20). Figure 2 shows the RMSE as a function of ν, for constant kernel shape parameter $\varepsilon = 30$ and for a fixed number $n = 1230$ of Radon lines (on a parallel beam geometry). We have observed that the minimal RMSE is attained at $\nu^* = 0.4522$ (cf. Figure 2). Note that the graph in Figure 2 illustrates the dependence between the RMSE and the weight parameter ν quite well.

We have further performed a series of rather extensive numerical experiments concerning the phantoms bull's eye, the crescent-shaped phantom, and the Shepp-Logan phantom, where our reconstructions were computed on a parallel beam geometry

with $N = 30$ angles and $2M + 1 = 41$ lines per angle, so that the number of Radon samples is $n = 1230$. Table 2 shows "optimal" combinations of values ε^* for the Gaussian kernel and ν^* for the Gaussian weight, whose resulting RMSE $\equiv$ RMSE(ε, ν) is minimal.

Phantom	kernel ϕ_ε	weight w_ν
crescent-shaped phantom	$\varepsilon^* = 19.66$	$\nu^* = 0.51$
bull's eye	$\varepsilon^* = 15.52$	$\nu^* = 0.45$
Shepp-Logan phantom	$\varepsilon^* = 18.28$	$\nu^* = 2.06$

Table 2: "Optimal" shape parameters for Gaussian kernel and Gaussian weight. Fine-tuning of shape parameter ε^* and weight parameter ν^* for three different phantoms by Gaussian reconstruction on parallel beam geometry (for $N = 30$ angles and $2M + 1 = 41$ lines per angle).

6.3 Comparison of Kernel-based Reconstructions on Parallel Beam Geometry

In Figure 3 we show a comparison between reconstructions from the three different kernels, where for each kernel, we have performed a fine-tuning of the method parameters ε and ν. For the Gaussian kernel, the "optimal" parameters ε^* and ν^* are in Table 2.

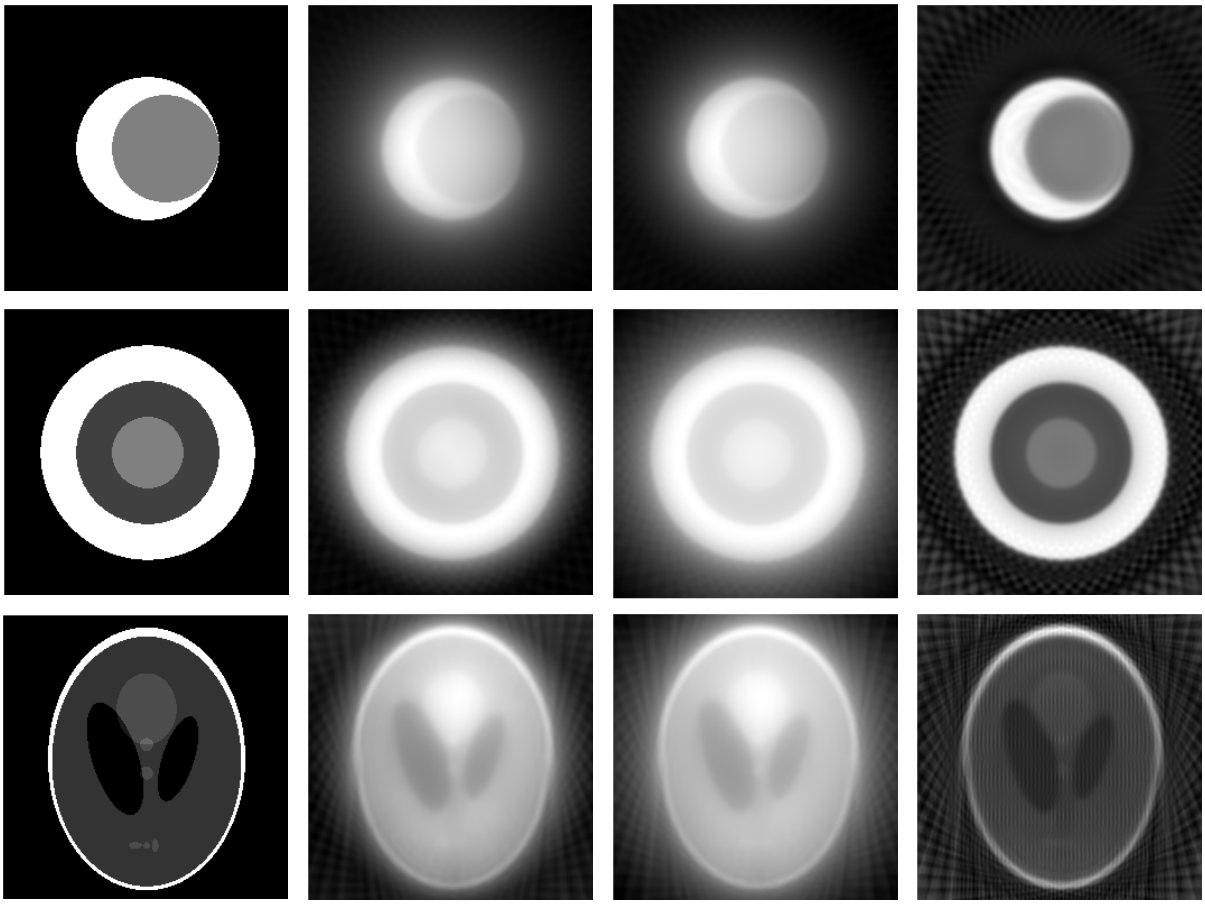

Figure 3: Kernel-based reconstructions on parallel beam geometry. The reconstructions are obtained from $n = 1230$ Radon samples, on a parallel beam geometry with $N = 30$ angles and $2M + 1 = 41$ lines per angle. The original phantoms (1st col), their reconstruction by inverse multiquadric (2nd col), by the compactly supported kernel (3rd col), and by the Gaussian kernel (4th col) are shown. The "optimal" values for the Gaussian parameters ε and ν are in Table 2.

On our numerical results of Figure 3 we can conclude that the reconstruction quality obtained from the Gaussian kernel is clearly superior to those obtained from the compactly supported and the inverse multiquadric kernel, provided that the Gaussian method parameters ε and ν are well-chosen. Note that the performance of the compactly supported kernel and the inverse multiquadric kernel is comparable. This complies with our numerical results, as documented in [14].

6.4 Kernel-based vs Fourier-based Reconstruction

We compare the proposed kernel-based Gaussian reconstruction method with Fourier-based reconstructions, relying on the filtered back projection formula (3), where we considered using the standard *Shepp-Logan* low pass filter, given as

$$A(\omega) = |\omega| \cdot \left(\frac{\sin(\pi\omega/(2L))}{\pi\omega/(2L)} \right) \cdot \chi_{[-L,L]}(\omega) = \begin{cases} \frac{2L}{\pi} \cdot |\sin(\pi\omega/(2L))| & \text{iff } |\omega| \le L; \\ 0 & \text{iff } |\omega| > L. \end{cases}$$

so that the filter $|S|$ in (3) is being replaced by $A(S)$. Note that $A(S) \approx |S|$ for small frequencies S.

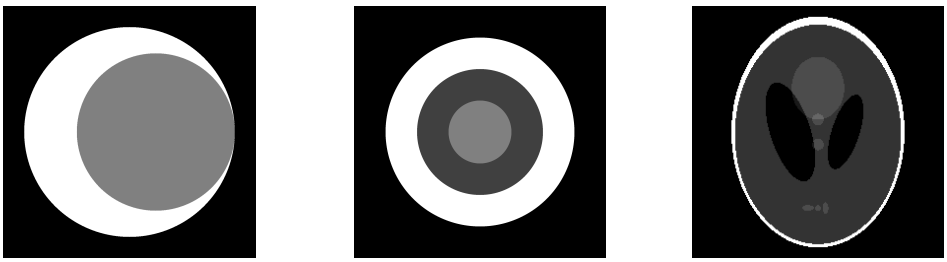

Crescent-shaped phantom **Bull's eye** **Shepp-Logan phantom**

Figure 4: Three popular phantoms. Crescent-shaped phantom, bull's eye, and Shepp-Logan (each of size 256×256).

We remark that the standard implementation of the Fourier-based filtered back projection formula (3) relies on a *regular* distribution of Radon lines. To this end, we work with a *parallel beam geometry*. In this case, by the discretization $\theta_k = k\pi/N$, for $k = 0, \ldots, N-1$, of the angular variable $\theta \in [0, \pi)$ and $t_j = jd$ (for some fixed sampling spacing $d > 0$), where $j = -M, \ldots, M$, for the radial variable $t \in \mathbb{R}$, the data acquisition relies on $(2M+1) \times N$ regularly distributed Radon lines ℓ_{t_j,θ_k}. Note that for any fixed angle θ_k, the Radon lines ℓ_{t_j,θ_k}, $-M \le j \le M$, are parallel (at uniform distance d and symmetric about the origin), which explains the naming *parallel beam geometry*. For illustration, Figure 5 (a) shows a set of $(2M+1) \times N = 110$ Radon lines ℓ_{t_j,θ_k} on parallel beam geometry, where we let $N = 10$, $M = 5$, and $d = 0.2$.

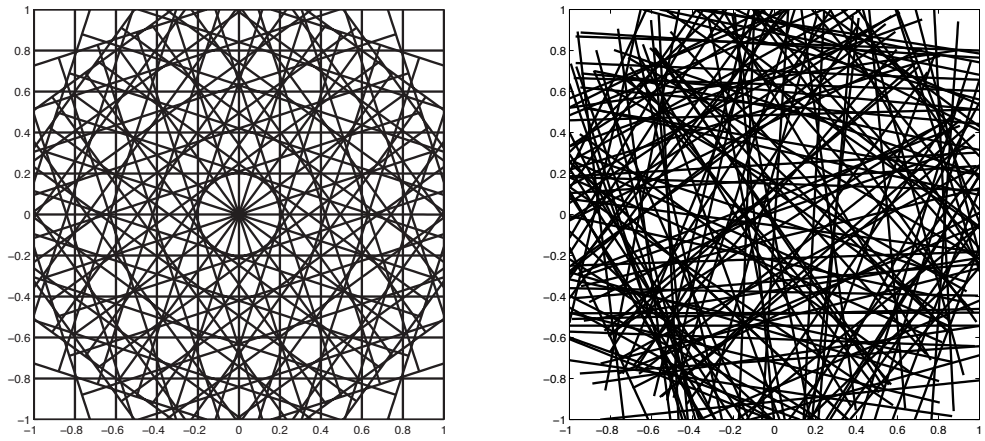

(a) Radon lines on parallel beam geometry **(b) Scattered Radon lines**

Figure 5: (a) Radon lines on parallel beam geometry. A set of 110 Radon lines ℓ_{t_j,θ_k} is shown, using increments of $\pi/10$ for the radial variable θ_k, i.e., $N = 10$, with $2M+1 = 11$ different Radon lines per angle, letting $t_j = jd$, for $j = -5, \ldots, 5$, at sampling spacing $d = 0.2$. **(b) Scattered Radon lines.** A set of 170 randomly distributed Radon lines ℓ_{t_j,θ_j} is shown, $j = 1, \ldots, 170$.

Now let us turn to our numerical comparisons between Fourier-based and kernel-based reconstructions. In each test case, we let $N = 45$ and $M = 40$, so that $(2M+1) \times N = 3645$ Radon samples are taken. In the kernel-based Gaussian reconstruction, we have used the "optimal" parameters shown in Table 2. The resulting reconstructions obtained from the two methods are displayed in Figure 6. Given our numerical results, we can conclude that our kernel-based reconstruction method is competitive to the Fourier-based reconstruction method, by the visual quality of their reconstructions and by the RMSE.

6.5 Reconstruction from Scattered Radon Data

Let us turn to the reconstruction from *scattered* Radon data. In our numerical experiments, we have generated sets of unstructured Radon lines by random, so that the geometry of the sample lines is unstructured. Figure 5 (b) shows one example for a set of 170 randomly distributed Radon lines in the domain $[-1, 1]^2$.

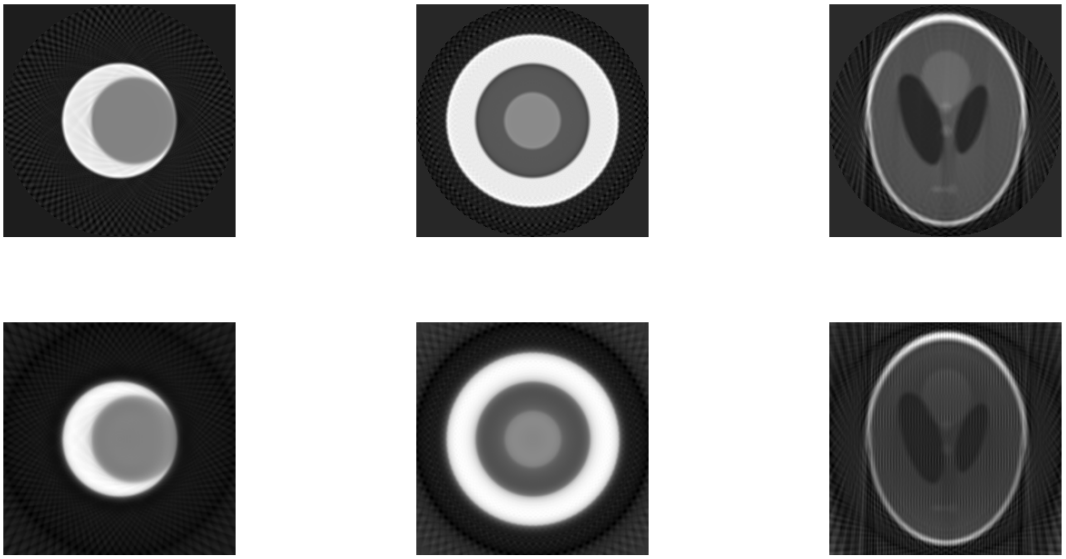

Crescent-shaped phantom **Bull's eye** **Shepp-Logan phantom**

Figure 6: Kernel-based vs Fourier-based reconstruction. For the phantoms crescent-shaped, bull's eye, and Shepp-Logan, their Fourier-based reconstructions (1st row) and kernel-based reconstructions (2nd row) are shown. The six reconstructions are computed from $(2M+1)\times N = 3645$ Radon samples (where we let $N = 45$ and $M = 40$) on parallel beam geometry, respectively. The corresponding root mean square errors (RMSE) are displayed in Table 3.

Table 3: Kernel-based vs Fourier-based reconstruction. For the reconstructions in Figure 6, their RMSE are shown.

Phantom	Kernel-based	Fourier-based
crescent-shaped	*0.10*	0.12
bull's eye	0.14	*0.13*
Shepp-Logan	*0.16*	0.18

We applied our kernel-based reconstruction method to a sequence of $n = 2000, 5000, 10000, 20000$ randomly chosen scattered Radon lines, taken from the phantoms bull's eye and crescent-shaped.

Figure 7 shows the obtained sequences of reconstructions, where in each test case we have used "optimal" shape parameters from Table 2. The corresponding RMSE values are shown in Table 4.

Although the geometry of the scattered Radon lines are visible in the displays of Figure 7, the basic features of the two phantoms are captured very well, where the reconstruction quality is improved as the number n of Radon samples increases.

Note that the RMSE values (in Table 4) are not monotonically decreasing. This is due to the random distribution of the scattered Radon lines, cf. Figure 7. Nevertheless, the global trend of the RMSE values is, at increasing n, monotonically decreasing.

Table 4: Scattered Radon lines. RMSE for kernel-based reconstructions in Figure 7, for $n = 2000, \ldots, 20000$ scattered Radon lines.

Phantom	2000	5000	10000	20000
crescent-shaped	0.15	0.14	0.14	0.12
bull's eye	0.19	0.17	0.21	0.19

7 Final Remarks and Conclusion

We developed a kernel-based image reconstruction method for scattered Radon data. The proposed reconstruction method relies on Hermite-Birkhoff interpolation by positive definite Gaussian kernels in combination with a regularization of the Radon transform by Gaussian weights. Our kernel-based reconstruction method is shown to be competitive with Fourier-based reconstructions from Radon data on parallel beam geometry. The main advantage of the proposed kernel-based reconstruction method is its enhanced flexibility. In fact, the kernel-based method can *unconditionally* be applied to arbitrary distributions of Radon lines. This is in contrast to classical Fourier-based reconstructions whose implementation relies on the filtered back projection formula.

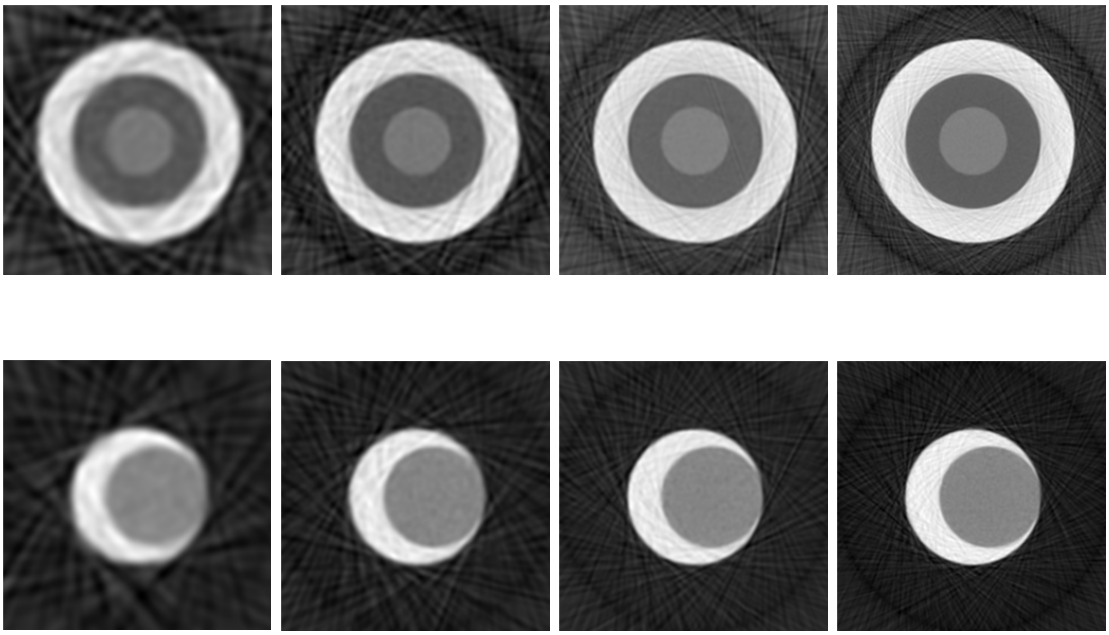

Figure 7: Kernel-based reconstruction from scattered Radon data. For the test cases bull's eye (first row) and crescent-shaped phantom (second row), a sequence of scattered Radon data is taken. The figure shows the corresponding reconstructions for an increasing number $n = 2000, 5000, 10000, 20000$ of scattered Radon samples (from left to right), obtained from the proposed kernel-based reconstruction method. The corresponding root mean square errors (RMSE) are displayed in Table 4.

References

[1] R. Askey: Radial characteristic functions. Technical Report, TSR # 1262, University of Wisconsin, Madison, 1973.

[2] Å. Bjørck: *Numerical Methods for Least Squares Problems*. SIAM, Philadelphia, 1996.

[3] S. Bochner: *Vorlesungen über Fouriersche Integrale*. Akademische Verlagsgesellschaft, Leipzig, 1932.

[4] W. Cheney and W. Light: *A Course in Approximation Theory*. Brooks/Cole, Pacific Grove, 2000.

[5] T.G. Feeman: *The Mathematics of Medical Imaging: A Beginner's Guide*. Second Edition. Springer Undergraduate Texts in Mathematics and Technology (SUMAT), Springer, New York, 2015.

[6] R. Gordon, R. Bender, and G. Herman: Algebraic reconstruction techniques (ART) for three dimensional electron microscopy and X-ray photography. Journal of Theoretical Biology **29**(3), 1970, 471–481.

[7] S. Helgason: *The Radon Transform*. Progress in Mathematics, vol. 5, 2nd edition. Birkhäuser, Basel, 1999.

[8] A. Iske: Reconstruction of functions from generalized Hermite-Birkhoff data. In: *Approximation Theory VIII, Vol. 1: Approximation and Interpolation*, C.K. Chui and L.L. Schumaker (eds.), World Scientific, Singapore, 1995, 257–264.

[9] A. Iske: Scattered data approximation by positive definite kernel functions. Rendiconti del Seminario Matematico **69**(3), 2011, 217–246.

[10] F. Natterer: *The Mathematics of Computerized Tomography*. Classics in Applied Mathematics, vol. 32. SIAM, Philadelphia, 2001.

[11] R.G. Novikov: An inversion formula for the attenuated X-ray transformation. Ark. Mat. **40**, 2002, 145–167.

[12] J. Radon: Über die Bestimmung von Funktionen durch ihre Integralwerte längs gewisser Mannigfaltigkeiten. Berichte Sächsische Akademie der Wissenschaften **69**, 1917, 262–277.

[13] R. Schaback and H. Wendland: Characterization and construction of radial basis functions. *Multivariate Approximation and Applications*, N. Dyn, D. Leviatan, D. Levin, and A. Pinkus (eds.), Cambridge University Press, Cambridge, 2001, 1–24.

[14] A. Sironi: *Medical Image Reconstruction Using Kernel Based Methods*. Master's Thesis, University of Padova, 2011. arXiv:1111.5844v1. `http://arxiv.org/pdf/1111.5844v1.pdf`.

[15] H. Wendland: *Scattered Data Approximation*. Cambridge University Press, 2005.